Research paper

Dissociation in strong field: A quantum analysis of the relation between angular momentum and angular distribution of fragments

Bar Ezra[a], Shimshon Kallush[a,b], Ronnie Kosloff[a]

[a] *The Institute of Chemistry and the Fritz Haber Centre for Theoretical Chemistry, The Hebrew University of Jerusalem, Jerusalem 9190401, Israel*
[b] *Department of Physics and Optical Engineering, ORT-Braude College, P.O. Box 78, 21982 Karmiel, Israel*

HIGHLIGHTS

- A method to simulate strong-field photodissociation of diatomic molecules was developed.
- Novel features of the model include:
- Carefully designed absorbing boundary conditions.
- Thermal initial conditions

ARTICLE INFO

ABSTRACT

An ab initio simulation of strong-field photodissociation of diatomic molecules was developed, inspired by recent dissociation experiments of F_2^-. The transition between electronic states was modeled with thermal initial conditions. Carefully designed absorbing boundary conditions were applied to describe the boundary conditions of the experiment. We studied the influence of field intensity on the direction of the outcoming fragments and laboratory-fixed axis, defined by the field polarization. At high intensities, the angular distribution became more peaked with a marginal influence on kinetic energy release. The study is the first step in a complete simulation of strong field control of photodissociation.

1. Introduction

High-intensity time-domain spectroscopy can be modeled by explicitly solving the time-dependent Schrödinger equation, for which knowledge of the full Hamiltonian of the process is essential. Employing the Born–Oppenheimer approximation, the Hamiltonian is separated into electronic and nuclear terms [1]. The nuclear degrees of freedom are represented by vibrational and rotational terms. Coupling the external electromagnetic field and the transition dipole moment, induces transitions between electronic states. Each electronic transition is accompanied by an angular momentum change of one unit of $\hbar$.

In this paper, we study strong-field spectroscopy of diatomic molecules [2]. The most studied molecule of these molecules is the diatomic anion I_2^-, which has been subjected to ultrafast photoelectron spectroscopy. Models describing its photoelectron distribution have been constructed under different approximations [3]. It is quite customary to neglect the rotational dependency of I_2^-, due to iodine's significantly heavy nuclei and slow dynamics within the *fsec* pulse time scales.

To include rotational effects a semi-analytical theory of photodissociation processes was first developed by Zare [4], and then further discussed and extended [5,6]. The semi-analytical assumptions include only one photon transitions. Hence, the results were suited to low-intensity radiation, where only single-photon processes are considered to lead to the dissociation of the molecule.

An extended theoretical treatment was developed by Ben-Itzhak, with Esry's collaboration, employing ab initio simulations to interpret the experimental results of H_2^+ photodissociation [7–9]. Initially, they considered only electronic and vibrational modes, assuming that the influence of the nuclear rotational states was negligible [7]. This assumption was revisited by Anis and Esry in a later study [8], where they concluded that the rotational states are essential. Note, that the initial state was set as the ground rovibrational state, practically setting the temperature to zero, an assumption that is justified for such species at low temperatures. Furthermore, they employed the Floquet dressed-states picture which is appropriate when the laser field is characterized

by a single frequency. The general issue of diatomic dissociation is currently active studied applying different approximations [10–14].

In this paper, we had two main goals: first, to acquire a more fundamental comprehensive understanding of the high-field dissociation process on a quantum scale; and second, to simulate the angular distribution of the photo-fragments resulting from this process. The current simulation uses the physical parameters of F_2^-. The motivation to use the F_2^- molecule as a benchmark follows from a recent experimental study by Strasser et al. [15,16]. Furthermore, its electronic structure is rather simple: there are only four low-lying states before reaching the detachment continuum. The photoelectron detachment channel is thus ignored, due to the 10 eV energy gap to the closest electronic state.

We present a first principle model, which includes a numerically exact solution of the time-dependent Schrödinger equation. All of the nuclear rotational and vibrational states, and the couplings between them, are included. We simulate a finite temperature ensemble, and therefore the initial state is thermal. The option of the Floquet dressed picture is not employed here for the reason that it is limited to relative long pules. The angular distribution of the fragments, as well as other observables, are extracted directly from the calculated wavefunction. We used the freedom of setting the model to explore fundamental processes and simplify the F_2^- system into a two-electronic-state system, presented in inset (b) Fig. 4. The simplified model an enable clear and informative bench-marking before going down the rabbit hole of the complete and details simulations of the photodissociation process.

2. Model

We consider a model of a diatomic molecule in the gas phase. The quantum dynamics takes place on n electronic states and three ro-vibrational internal nuclear degrees of freedom. The spin was assumed to be zero, and thus does not contribute to the system complexity.

The Hamiltonian of the system contains the nuclear Hamiltonian of all of the electronic states, and coupling elements between the states due to the transition dipole moment. The Hamiltonian in a Born–Oppenheimer expansion [1] of electronic and nuclear coordinates becomes:

$$\hat{H}_{sys} = \sum_n \left(\hat{H}_n \otimes |n\rangle\langle n| + \sum_{k \neq n} \boldsymbol{\mu}_{n,k} \cdot \boldsymbol{\varepsilon} \otimes |n\rangle\langle k| \right) \tag{1}$$

where $\hat{H}_n$ is the nuclear Hamiltonian operator of the electronic state n, $\boldsymbol{\mu}_{n,k}$ is the transition dipole operator between the states n and k, and $\varepsilon(t)$ represents the laser field. Note that both ε and $\boldsymbol{\mu}$ are vectors, and the scalar product between them results in different transition schemes, which depend on the involved states' symmetries and the field polarization. In cases where the transition between the states is forbidden, the dipole element vanishes. Non-adiabatic coupling can be added to the Eq. 1. The nuclear Hamiltonian of each electronic state can be written as

$$H_n = \frac{\hat{P}_r}{2m_r} + V_n(r) + \hat{H}_{rot}(r) \tag{2}$$

where r is the internuclear distance, $\hat{P}_r$ is the corresponding momentum, m_r is the nuclear reduced mass, $V_n(r)$ is the electronic potential of the state n, and $\hat{H}_{rot}$ is the rotational Hamiltonian. The molecular and linearly polarized laser field axes define the internuclear axis, $\hat{z}$, and the laboratory axis, $\hat{Z}$, respectively.

The rotational Hamiltonian is

$$\hat{H}_{rot}(r) = B(r)\hat{\boldsymbol{R}}^2 \tag{3}$$

where $B(r)$ is related to the moment of inertia, $B = \frac{1}{2\mu r^2} = \frac{1}{2I}$ and $\hat{\boldsymbol{R}}$ is the nuclear rotational angular momentum operator, equal to $\hat{\boldsymbol{R}} = \hat{J} - \hat{L} - \hat{S}$; $\hat{J}$ is the total angular momentum of the molecule, $\hat{L}$ is the electronic orbital angular momentum, and $\hat{S}$ is the electronic spin

angular momentum.

In Hund's case (a) [17] – the most common case and the one used here, $\hat{L}$ and $\hat{S}$ are coupled to the internuclear axis, $\hat{z}$, and the projections on it are Λ and Σ, respectively. The projection of $\hat{J}$ on the laboratory axis, $\hat{Z}$, is m and on the internuclear axis, $\Omega = \Lambda + \Sigma$.

2.1. Basis set representation

The state of the molecule is described by a nuclear and an electronic state. In the present work, we concentrate on cases in which all electrons are paired, and therefore the spin quantum number is $\hat{S} = 0$. In this situation, the projection of the electronic orbital angular momentum on the internuclear axis is similar to the total projection, $\Lambda = \Omega$.

The internuclear degree of freedom of the molecule is described by r, the distance between the atoms. The orientation is defined by the angles θ and ϕ, expanded in terms of the Wigner rotation matrix, $D^j_{m,\Omega}(\phi, \theta)$. At $\Omega = 0$, the matrices are equal to spherical harmonics functions, $Y_{j,m}(\phi, \theta)$. In this basis set each state is described by different r, j, m and Ω values.

The molecular state at time t can be written by the density matrix:

$$\rho(r, r', \theta, \theta', \phi, \phi', n, n';t) = \sum_{\zeta,\zeta'} |n\rangle\langle n'| \otimes a_{\zeta,\zeta'}(r, r';t) \otimes |\zeta\rangle\langle\zeta'| \tag{4}$$

where $|\zeta\rangle$ is the wavefunction with the quantum numbers $|j, m, \Omega\rangle$, expanded by the $D^j_{m,\Omega}$ matrices.

2.2. Coupling elements

The coupling elements are calculated by vector multiplication between the laser field $\varepsilon(t)$ and the transition dipole between the electronic states, $\boldsymbol{\mu}$. The transition dipole elements depend on the symmetry, Σ or Π, and the parity, Gerade or Ungerade, of the states.

For a linearly polarized field, the rotational coupling elements are given by:

$$\langle\zeta'|\mu_{0q}\varepsilon_0|\zeta\rangle \propto \int D^{j'\,*}_{m'\Omega'}(\theta, \phi, 0)\, D^1_{0q}(\theta, \phi, 0)\, D^j_{m\Omega}(\theta, \phi, 0)\, d\Omega$$

$$= 8\pi \begin{pmatrix} j & 1 & j' \\ -m & 0 & m' \end{pmatrix} \begin{pmatrix} j & 1 & j' \\ -\Omega & q & \Omega' \end{pmatrix} \tag{5}$$

where μ_{0q} is the transition dipole moment proportional to $D^1_{0q}(\theta, \phi, 0)$ [18]. The value of q is determined for a given transition case and is equal to $q = \Omega - \Omega'$.

The first term is the initial state $D^{j'}_{m',\Omega'}(\theta, \phi)$, the second term is the coupling operator of the transition $D^1_{0q}(\theta, \phi)$, and the third term is the final state $D^j_{m,\Omega}(\theta, \phi)$. The coupling components are calculated by the given $3 - j$ symbols.

We will consider two transition cases:

- Transition between two Σ electronic surfaces: in this case, $q = 0 - 0 = 0$ hence the coupling D matrix is D^1_{00}. Note that the transition between two Π electronic surfaces gives the same coupling elements, $q = 1 - 1 = 0$.
- Transition between Σ and Π electronic surfaces: in this case, $q = 1 - 0 = 1$, hence the second D matrix is $D^1_{0\pm1}$.

For the two cases:

$$\boldsymbol{\mu} \cdot \boldsymbol{\varepsilon} \propto \begin{cases} \mu\varepsilon\, D^1_{00}(\theta, \phi) \propto \cos(\theta) & \Sigma - \Sigma \\ \mu\varepsilon\, D^1_{0\pm1}(\theta, \phi) \propto \sin(\theta) & \Sigma - \Pi \end{cases} \tag{6}$$

In all the calculations, we assumed that μ is independent in the internuclear distance r.

Additional insight into these results can be obtained by decomposing the transition dipole into a component in the internuclear direction $\mu_\parallel$ and a component in the perpendicular direction $\mu_\perp$. The
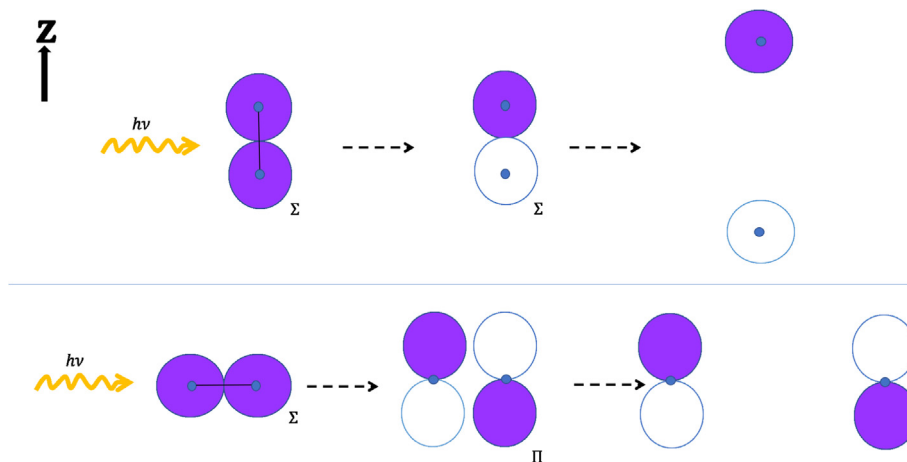
Fig. 1. The two transition cases - semi-classical illustration. **Upper panel**: transition between two Σ electronic surfaces. Starting at a bound electronic surface, Σ_g, the laser excites to the un-bounding electronic surface, Σ_u, then the molecule dissociated. The fragments are obtained in the direction of the polarization of the light. **Lower panel**: Transition between Σ and Π electronic surface. Starting at a bound electronic surface, Σ_g, the laser excites to the un-bounding electronic surface, Π_u, then the molecule dissociated. The fragments are obtained in the perpendicular direction to the polarization of the light.

scalar product between the transition dipole and the field becomes:

$$\mu \cdot \varepsilon = \varepsilon(\mu_{\parallel}\cos\theta + \mu_{\perp}\sin\theta) \tag{7}$$

Therefore, the transition dipole is parallel in the first case and perpendicular in the second case to the internuclear direction. An illustration of the two coupling cases is presented in Fig. 1.

The transition between the electronic states changes the total angular momentum state. For linearly polarized light, the projection of the laboratory axis m on the Z spatial axis is conserved. The quantum number Ω can change with the change in value of q, depending on the transition case. The quantum number j changes by one unit of angular momentum $\hbar$ or remains the same (Q branch at the $\Sigma - \Pi$ transition).

2.3. Initial state

The model is constructed to mimic a hypothetical experiment: a molecular beam with a fixed temperature is subjected to a pulsed laser source. The ensemble's temperature was taken to correspond to the initial state of F_2^- at 20 K. At this temperature, the electronic and vibrational degrees of freedom are in their ground state. The initial state can be written as follows:

$$\rho(t = 0) = \rho_{electronic} \otimes \rho_{rovibration} \tag{8}$$

where $\rho_{electronic} = |\psi_0^e\rangle\langle\psi_0^e|$. The vibrational projection is conditioned on the rotational quantum number j, $\rho_{rovibration} = P_{0,j}(r) = |\Phi_{n=0,j_i}(r)\rangle\langle\Phi_{n=0,j_i}(r)|$. The vibrational ground state for each value of j is obtained by imaginary time propagation [19], independently for each j. Note that the vibrational wavefunction can be different for different quantum numbers.

The initial rovibration state is a Boltzmann distribution of several rotational components.

$$\rho_{rovibration} = \frac{1}{Z}\sum_{\zeta_i}(2j_i + 1)exp(-\beta E_{j_i})P_{0,j}(r)|\zeta_i\rangle\langle\zeta_i| = \sum_{\zeta_i}\xi(j_i)P_{0,j}(r)|\zeta_i\rangle$$
$$\langle\zeta_i| \tag{9}$$

where $\xi(j_i)$ is the normalized probability for state j_i with the partition function $Z = \sum_l (2l + 1)exp(-\beta(E_l))$. $E(j_i)$ are the rotational energy eigenvalues, $\hat{H}_{rot}|\psi_{\zeta_i}\rangle = E(j_i)|\psi_{\zeta_i}\rangle$, that depend only on the total angular momentum j as explained above. The index i describes the initial quantum numbers of the state and will be used in this notation from this point on.

The total initial state is:

$$\rho(r, r, \theta, \theta', \phi, \phi', n, n'; t = 0) = \sum_{\zeta_i}\xi(j_i)a_{\zeta_i,0,\zeta_i,0}(t = 0)\cdot|0\rangle$$
$$\langle 0| \otimes P_{0,j}(r) \otimes |\zeta_i\rangle\langle\zeta_i| \tag{10}$$

2.4. Propagation in time

The dynamics of the state is carried by a first principle approach. The evaluation of the state is described by a unitary transformation:

$$\rho(t) = \hat{U}(t)\hat{\rho}(t = 0)\hat{U}^{\dagger}(t) \tag{11}$$

where $\hat{U}(t)$ is the propagator which is generated by the time-dependent Schrödinger equation:

$$i\hbar\frac{d}{dt}\hat{U}(t) = \hat{H}(t)\hat{U}(t) \tag{12}$$

and the Hamiltonian is the generator. The density operator, $\rho(t)$, provides all observable data. For example, the observable result that corresponding to the operator $\hat{A}$, will be calculated as follows:

$$\langle\hat{A}\rangle_t = tr(\hat{A}\rho(t)) = tr(\hat{A}\hat{U}(t)\rho(t = 0)\hat{U}^{\dagger}(t)) \tag{13}$$

Under common molecular beam conditions, typical incoherent processes such as collisions or spontaneous decay take place on the time scales of $t \geqslant 1$ nsec. The dissociation process is completed by ~ 100 fsec. We can therefore assume that the dynamics is fully coherent. The expectation values can be evaluated by using the basis where the initial density operator is diagonalized $|\widetilde{\psi}_{n,\nu,i}\rangle = |\psi_n^e\rangle \otimes |\psi_{\nu}^{\nu}\rangle \otimes |\zeta_i\rangle$), giving:

$$\langle\hat{A}\rangle_t = \sum_{n,\nu,i}\langle\hat{U}^{\dagger}(t)\widetilde{\psi}_{n,\nu,i}(t = 0)|\hat{A}|\hat{U}(t)\widetilde{\psi}_{n,\nu,i}(t = 0)\rangle \tag{14}$$

Eq. 14 can be decomposed into the expectation values of the individual components. Each component requires the solution of the time-dependent Schrödinger equation for a wavefunction: $i\frac{d}{dt}\psi = \hat{H}(t)\psi$, which is then computed by employing short time steps and solving for each step by the Chebyshev approximation [20–22] assuming that $\hat{H}(t)$ is piecewise constant. The basic evaluation of $\hat{H}\phi$ for Eq. 1 is carried out using the Fourier grid method for the internuclear coordinate r [23,24] and angular momentum algebra for the rotation. Details of the parameters are given in Table 1.

The propagation is therefore decomposed into independent wavefunctions. The initial state for a wavefunction representation becomes:

$$|\Psi_i(r, \theta, \phi; t)\rangle = \sqrt{\xi(j_i)}\sum_{n,\zeta}\sqrt{a_{\zeta,n,\zeta,n}(t)}|\Phi_{n,\zeta}(r;t)\rangle \otimes |n\rangle \otimes |\zeta\rangle \tag{15}$$

Table 1
Model parameteres

parameter	value
μ-reduce mass of F_2^-	9.5 amu
Bond length	6.8 Angstrom
Rotational Constant	8.88 cm^{-1}
Δr	0.0464 bohr
Δt	$5 \cdot 10^{-2}$ fsec
Pulse width	30 fsec
Central wavelength	320–390 nm
Intensity	$10^{11} - 10^{16} \frac{W}{cm^2}$
$\bar{\mu}$- dipole moment	0.2 au
Electronic potentials	private communication
Temperature	20 K

2.5. Absorbing boundary condition

In a typical photodissociation experiment, the fragments are detected far from the dissociation point. At the detection point, the particles are characterized by their momentum, which is detected by velocity map imaging [25,16]. Comparable information can be calculated by the asymptotic momentum, amplitude, and direction, at far internuclear distance. We can employ the fact that the position information is not detected and restrict the computation grid in r up to the region where the potential becomes flat. To extract the direction, the phase information must be conserved, since the wavefunction is encoded in angular momentum components and not in direction.

To achieve these goals, we constructed an auxiliary grid in r for each wavefunction component. This grid is flat with potential energy matching the asymptotic potential of the primary grid. The two grids overlap in the asymptotic flat part of the primary grid. At constant time intervals τ, a portion of the asymptotic part of the wavefunction is moved to the auxiliary grid. This is achieved by a smooth transfer function which eliminates spurious reflections. This decomposition is possible due to the linearity of the wavefunction $\Psi = \Psi_{primary} + \Psi_{aux}$. Both wavefunctions are propagated simultaneously. The auxiliary wavefunction is stored in momentum space where the time propagation is just a phase shift by $\hat{U}(t) = \exp(-\frac{i}{\hbar}\frac{\hat{P}^2}{2m}t)$.

At the end of the propagation, all of the dissociated portion of the wavefunction is stored in the auxiliary grid:

$$\Psi_i(r, \theta, \phi; t = t_{final}) = \sum_{n_\tau} \sum_{\eta,\zeta} |\eta\rangle b_{\zeta,\eta}^i(r; n_\tau)|\zeta\rangle \qquad (16)$$

where n_τ is the time index for the wavefunctions that are transferred at different times, η denotes the auxiliary surface (corresponding to the

coupled surface n), and we composed the coefficients and the dependency of r. More information describe at the appendix section Appendix A.

All of the observables are calculated based on Eq. 14, which can be decomposed to individual wavefunction propagations, leading to the final state, Eq. 16. The thermal average observables are obtained by summation over the individual thermal components calculated for different initial states.

$$\langle A \rangle = \sum_i \langle A \rangle_i \qquad (17)$$

When more than one excited state potential is included, each channel is calculated separately.

The next sections contain the results of several calculations, for description for each observable see appendix section Appendix B. The model was set with the parameters from Table 1.

3. Theoretical analysis of experimental observables

The model is designed to provide a full description of a photodissociation experiment in a strong laser field. The system is initiated in a thermal state. The initial state resides on the ground bounded electronic and vibronic states with a thermal distribution of rotational states. The external pulse field couples the rotational states in the ground electronic to rotational states in the excited un-bounded electronic states. We systematically increased the radiation intensity to gain insight on strong field effects.

In all calculations, the ground electronic state was set as the singlet Σ bound electronic surface. The excited electronic surface was set to either Σ singlet or Π singlet with the same potential form. In all simulations, the electromagnetic-radiation was chosen to be a transform limited Gaussian pulse with a width of 30 fs. Wavelengths and intensities were varied.

3.1. Σ excited electronic surface

We first examine the dissolution outcome of radiation coupling two Σ electronic surfaces. Fig. 2a presents the angular distribution of the fragments' momentum in the parallel and perpendicular directions with respect to the polarization. For the weak field one-photon transition in a parallel excitation, the resulting distribution resides mainly in the parallel direction, and is proportional to $\cos^2(\theta)$, as expected.

Fig. 3 presents the dissociation probability as a function of wavelength. Neglecting spontaneous emission, the dissociation probability is equal to the excited state population. The excited state population is also proportional to the absorption energy [26,27] $\hbar\omega\Delta N = \Delta E$. By
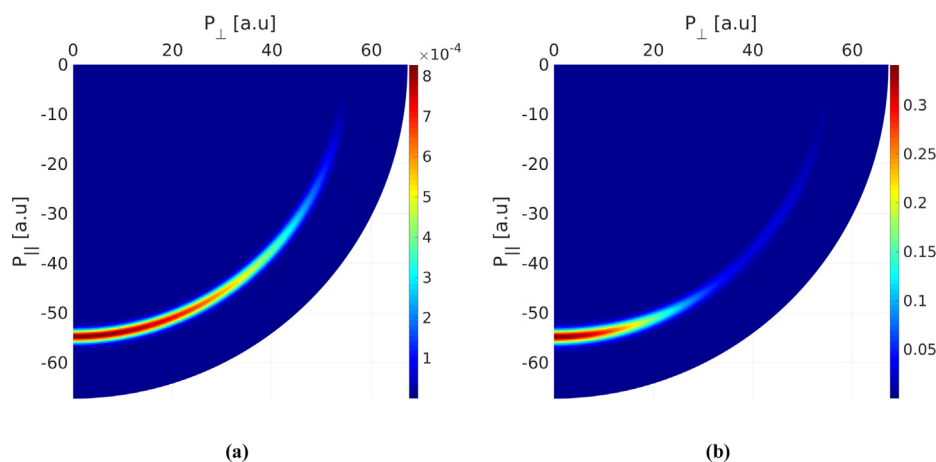

(a)   (b)

Fig. 2. Angular distribution of the outgoing momentum shown as a density plot. The results are for fragments emitted from the transition between two Σ electronic surfaces with different intensity, (a) low intensity- $I = 10^{10} \frac{W}{cm^2}$, (b) high intensity - $I = 10^{16} \frac{W}{cm^2}$.
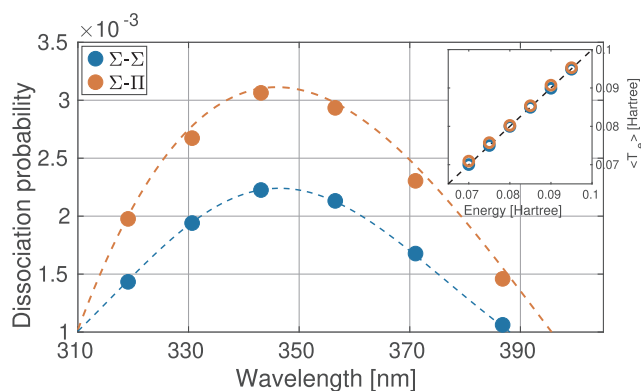
Fig. 3. Action spectrum represent the dissociation probability as function of wavelength for $\Sigma - \Sigma$, blue data, and $\Sigma - \Pi$, red data, electronic transfer. The action spectrum calculated with high intensity in the one photon transition range, $1 \cdot 10^{11}$ [W/cm^2]. The inset: Average kinetic energy of the photo-fragments, $\langle T_e \rangle$, as a function of Condon energy. The Condon energy is defined as the vertical energy minus the dissociation energy.

fitting the action spectrum (dashed line), we conclude that the peak of the transition is at 346 nm.

The coupling between the ground state and the excited state depends on the laser wavelength, which determines the Condon point. The Condon point is defined as the radius in which the two coupled potentials cross for a given vertical resonance energy. The vertical resonance energy value is the Condon energy. The inset in Fig. 3 displays the correlation between the fragments' average kinetic energy at different wavelengths and the corresponding Condon energy.

Nonlinear multi-photon processes develop when the laser intensity is increased. To explore these processes, we carried out a series of calculations with increasing pulse intensity. The simulations were conducted with the same wavelength, close to the peak of absorption.

Fig. 4 presents the dissociation probability as a function of laser intensity. The figure includes results of Σ and Π excited electronic states (see forward). For the case of an Σ excited electronic state, the dissociation probability increases with the laser intensity and saturates. The inset (a) in Fig. 4 presents the dissociation probability for low field intensity. As expected, the dissociation probability is linear with the intensity, fitted in the inset (a) by a black line. Note that a *log–log* scale was used for the main frame, while a linear one was used for the inset (a).

The number of photons involved in the process reshapes the angular distribution. Each photon transition multiplies the distribution by
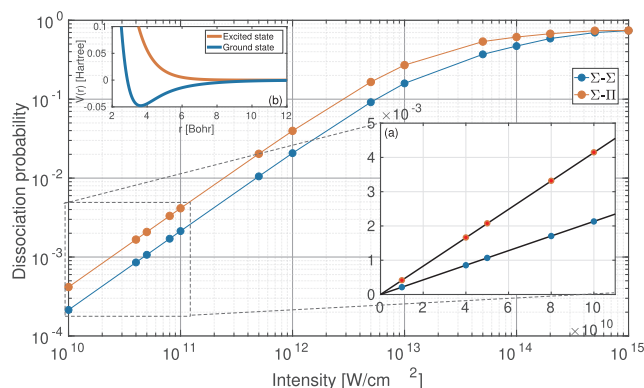

Fig. 4. Dissociation probability as a function of laser intensity for $\Sigma - \Sigma$ and $\Sigma - \Pi$ transition in blue and in red respectively. The intensity and the dissociation probability are presented in logarithmic scale. Inset (a): the linear range, linear fit to the data at black line. Inset (b): Electronic state potentials surfaces.The excite state, red, is chosen as either Σ or Π. These potentials represent the computed σ_u and σ_g state taken from [28].

$\cos^2(\theta)$. Therefore, for example at the three-photon transition, excitation–emission–excitation, the angular distribution becomes proportional to $\cos^6(\theta)$. Considering the DC component of the distribution, the outcome distribution form three-photon transition has a component of $\cos^4(\theta)$.

The full angular distribution can be written as a series of Legendre polynomials $P_N(\cos(\theta))$, each one caused by different number of photons transition. The series is forgathered at the highest photon transition of the process. Therefore, fitting the angular distribution to a polynomial series indicates the highest multi-photons transition in the process.

$$p(\theta; P) = \sum_{N=2,4,6..} \alpha_N(P) P_N(\cos(\theta)) \tag{18}$$

An example of angular distribution at high intensity is presented in Fig. 2b. Here, the stronger coupling with the field leads to a concentration of the probability in the parallel direction. This observation fits the classical intuition: when modulation in a particular direction, the dissociation becomes selective in this direction.

The difference between the angular distribution at different intensities can be examined by fitting the distribution at the most probable momentum, $P_{mp}(\theta)$. Fig. 5a presents the coefficients of $N = 2$ to $N = 10$ for the Σ excited electronic state as a function of laser intensity. The fitting was done using a Fourier transform to expand the angular distribution to 2π.

Increasing the intensity has a small effect on the kinetic energy of the fragments. Fig. 6 presents the mean value and the variance of the kinetic energy release (KER) for different laser intensities. The KER, for the transition between two Σ states (solid blue line), initially decreases with the intensity. This could be a result of the photon-locking process. At very high intensity, we observe an increase in the KER accompanied by a narrow distribution. The order of change in the KER is from low intensity to $1 \cdot 10^{15}$ [W/cm^2] is $\sim 0.1\%$.

It is essential to note that the extremely high intensities shown are beyond the validity of the Born–Oppenheimer model employed.

3.2. Π excited electronic surface

The quantum number Ω changes during the $\Sigma \rightarrow \Pi$ transitions. As explained in the previous section, at the Σ electronic surface $\Omega = 0$, whereas at the Π electronic surface, $\Omega = \pm 1$. Since each excited state level is now doubly degenerate, and the *Q branch* is allowed, each rotational state in the ground electronic surface is coupled to six states in the excited surface. In this case, the angular distribution of the fragments is expected to be proportional to $\sin^2(\theta)$ for one-photon transitions.

Fig. 7a presents the angular distribution of the fragments. A comparison to Fig. 2a reveals that the center of the momentum distribution, and thus the average kinetic energy, is similar for the two symmetries.

The dissociation probability is influenced by the change of in the excited electronic surface to Π. The dissociation probability as a function of the intensity is presented in Fig. 4. The slope at low intensities, the inset (a) in Fig. 4, is larger compared to the previous case of on Σ electronic surface, this was also observed by Csehi et al. [29]. The explanation to this observable is the larger number of excited states, at Π state case, that are coupled to each ground state. Furthermore, this change impacts the saturation intensity of the dissociation probability.

In the $\Sigma - \Pi$ transition, each absorbed photon multiplies the distribution by $\sin^2(\theta)$. This can be compared to the $\Sigma - \Sigma$ case where each absorbed photon multiplies the distribution by $\cos^2(\theta)$. It is customary to fit the angular distribution to $I(\theta) = 1 + \beta P_2(\cos(\theta))$. For single-photon excitation, this is also the appropriate form for $\Sigma \rightarrow \Pi$ transition. For multi-photon transition this form cannot fit the results. Therefore, the angular distribution was fitted to a polynomial series in $P_N(\sin(\theta))$, which for even N can be written also as $1 - P_N(\cos(\theta))$. Fig. 7b presents the results for coupling between the Σ and Π electronic

(a) Σ excited electronic state. $P_N\left(\cos\left(\theta\right)\right)$ (b) Π excited electronic state. $P_N\left(\sin\left(\theta\right)\right)$
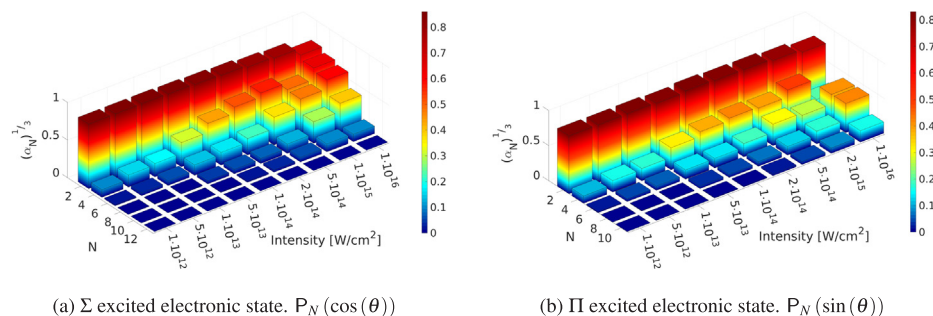
Fig. 5. The coefficients of fitting the angular distribution into a polynomial function as function of the intensity and the fitting order. The fitting is done to polynomial function of Legendre polynomials. Note, the coefficients display after cube root for convenience only.
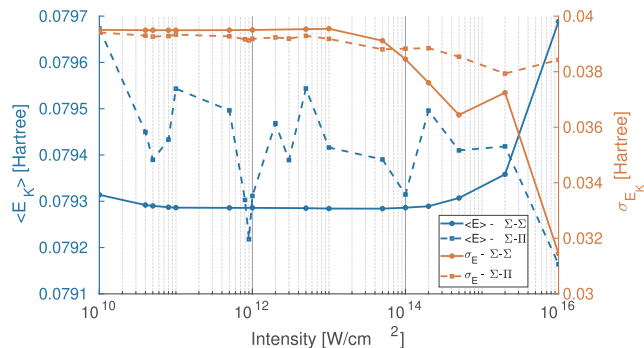

Fig. 6. The average kinetic energy release, solid line, and its variance distribution, dashed line. The figure separate to two Y axis, left for the average kinetic energy and the right for the variance distribution. The figure include data of $\Sigma - \Sigma$ transition, in blue, and of $\Sigma - \Pi$ transition, in red. (For interpretation of the references to color in this figure legend, the reader is referred to the web version of this article.)

states with high-intensity laser.

$$p(\theta;P) = \sum_{N=2,4,6..} \alpha_N(P)P_N(\sin(\theta)) \tag{19}$$

Fig. 5b presents the coefficients of $N = 2$ to $N = 10$ for the Π excited electronic state as a function of the laser intensity and the fitting order. By comparing this result to those of the Σ excited state, Fig. 5a, we conclude that the multi-photon transition is achieved at a higher intensity for the Π excited state. This difference is a result of the larger effective Hilbert space for the Π excited state.

The KER observations for the transition between Σ and Π states are

presented in Fig. 6 (dashed blue line). The KER shows non monotonic variations compered to the smooth dependence on intensity for the two Σ states. In addition, the overall variation is larger, $\sim 0.6\%$ but still quite small. This behavior could be a result of interference between the excitation pathways in a strong field.

4. Discussion and conclusion

The presented model for the photo-dissociation process is based on the exact solution of the time-dependent Schrödinger equation. Our survey of existing models of photodissociation showed that they typically employ very limiting simplifying assumptions. In this paper, we present a new model that aims to describe generic model systems, comparing different electronic state symmetries. The model contains a description of the nuclear rotational motion, and the coupling elements between rotational states.

Using this model, we presented the dissociation outcome for two processes, the transition between the Σ singlet electronic state to the Σ or Π singlet electronic state. For each case, we simulated the final momentum distribution of fragments. For weak-field one-photon transitions, we observed a momentum distribution proportional to $cos^2(\theta)$ for the $\Sigma - \Sigma$ transition and $sin^2(\theta)$ for the $\Pi - \Sigma$ transition. This is in accordance with previous models[4,6,9] based on perturbation theory. A detailed inquiry into the differences between the velocity maps for the two cases reveals that in the mainly parallel cosine transition the probability to dissociate at the perpendicular direction vanishes. For the second case, the probability to excite in the non-classical direction remains non-zero for all intensities. As was shown and explained by Csehi et al. [14], this results from symmetry of the occupied J states during the transition.
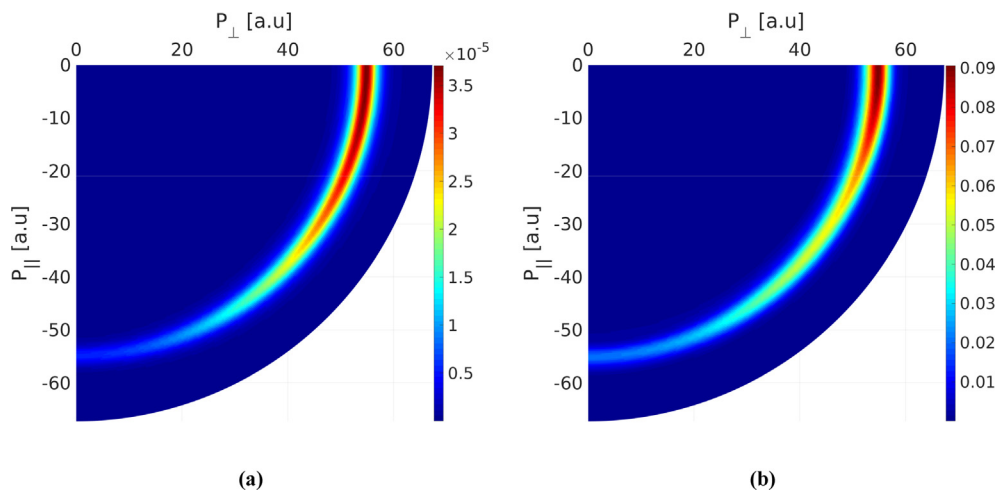

Fig. 7. Angular distribution of the outgoing momentum shown as a density plot. The results are for fragments emitted from the transition between Σ and Π electronic surfaces with different intensity, (a) low intensity- $I = 10^{10}\,\frac{W}{cm^2}$, (b) high intensity - $I = 10^{16}\,\frac{W}{cm^2}$.

Our new model simulates high-laser-intensity processes that lead to multi-photon transitions. We showed that the main effect of increasing the number of photons involved in the process reshapes the angular distribution. For parallel transitions, the angular distribution becomes sharper, indicating a more aligned distribution. In addition, the average KER and its distribution are only weakly dependent on the laser intensity.

In conclusion, we constructed a new model that can describe form first principle diatomic dissociation a wide range of radiation intensity. We advocate the view that the key to understanding a complex dynamical system is to rely on experience gained from small and simple models. Therefore, the results here are presented for two transition cases, between two Σ states and between Σ and Π states. Consistent with prior knowledge, the main difference between the two cases is the angular distribution symmetry. Furthermore, our new model shows that the threshold on the intensity were multi photon transition occur is lower in the Σ excited state then in the Π case.

Our model opens the way to explore the dissociation process of systems with high complexity. For simplicity, the current model introduces singlets as its electronic states. In future studies, we will describe the system using doublet states, which are more suitable to the F_2^- case. Moreover, spin effects should be taken into account, such as spin–orbit interactions. One might also notice that the model takes advantage of a lower temperature to reduce the size of the required

Hilbert space. Higher temperature enlarges the number of potentially populated rotational states, resulting in a larger Hilbert space. Such a simulation will require modified methods such of the use of random phase wavefunction[30]. Furthermore, employing coherent control can lead to new and fundamental results[12,31].

CRediT authorship contribution statement

Bar Ezra: Methodology, Software, Writing - original draft. **Shimshon Kallush:** Supervision. **Ronnie Kosloff:** Supervision.

Declaration of Competing Interest

The authors declare that they have no known competing financial interests or personal relationships that could have appeared to influence the work reported in this paper.

acknowledgements

Appendix A. Absorbing boundary conditions

To minimize computation effort the computation grid has to be cut at a predetermined radius. Since we want to analyze the outgoing asymptotic data, we cannot use the common option of absorbing the wavefunction at the end of the grid [32,33]. As an alternative we employ an auxiliary grid which overlaps the primary grid which we term transition window. The position of this window is optimized to minimize the primary grid without damaging the momentum distribution. The average kinetic energy is then calculated for different window radius points. Fig. 8 presents the average kinetic energy as a function of the window's starting radius. The propagation of the state at the auxiliary surface is a free propagation; hence the momentum distribution will not change with time for large *r*. Therefore, the part that absorbs at each time can be restored independently.

The total dynamical calculation was stopped when at least 99% of the excited state population moved to the auxiliary surface.

Appendix B. Theoretical analysis - observables

For each excited electronic surface we calculated the dissociation probability on the corresponding virtual surface η. The accumulated probability for initial state i

$$\mathscr{P}_{i,\eta} = \langle \Psi_{i,\eta}(r, \theta, \phi; t = t_{final}) | \Psi_{i,\eta}(r, \theta, \phi; t = t_{final}) \rangle = \tag{20}$$

$$= \int_0^\infty r^2 dr \sum_{m,\Omega,\tau} \left| \sum_j b_{\zeta,\eta}^i(r;\tau) \right|^2$$

$\mathscr{P}_{i,\eta}$ is a joint probability starting in initial state i and dissociation at electronic state η. Note that the wavefunction is normalized with Boltzmann coefficients. The first summation, over the quantum number j, is due to the coherence between different components of a given initial thermal state.

Asymptotically the total dissociation probability is equal to the missing probability at the ground state, this was been verified for consistently.

The momentum angular distribution is proportional to the experimental velocity distribution. The calculation requires to change the representation from the radial degree of freedom to the corresponding momentum, the change is done by using Fourier transform. Additionally, each
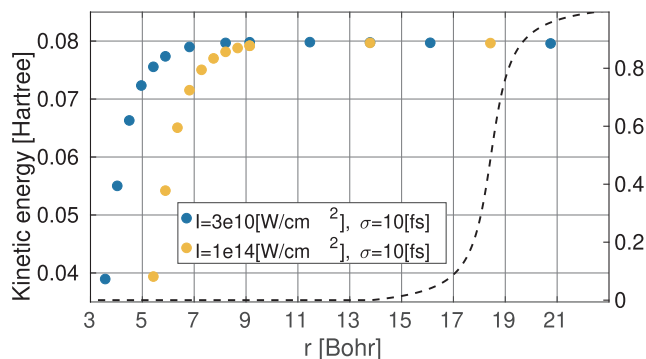

Fig. 8. Left axis: Final average kinetic energy calculated for different final states as a function of the starting position of the transfer window. Right axis: Represents the transfer operator between the grid *n* to the respectively auxiliary grid.

rotational state is explicitly written in the angular variables.

$$\widetilde{\psi}_i(p, \theta, \phi; t = t_{final}) = \sum_{\eta, \zeta} \sum_{\tau} \widetilde{b}^i_{\zeta, \eta}(p; \tau) \cdot |\eta\rangle \cdot D^j_{m, \Omega}(\theta, \phi)$$

(21)

It is important to notice that in the momentum representation, there is a relative phase between different virtual time parts, τ.

The distribution of each virtual surface and initial state is calculated as follows:

$$\mathscr{D}_{i,\eta}(p, \theta, \phi) = \sum_{m, \Omega} \left| \sum_j \left(\sum_\tau \widetilde{b}^i_{\zeta, \eta}(p; \tau) \right) \cdot D^j_{m, \Omega}(\theta, \phi) \right|^2$$

(22)

The summation over j is a quantum summation and conserve phases, due to the coherence between different values that generate during the dynamic. In contrary, the summation over m and Ω are classical since there are no physical coherences between different values.

$$\mathscr{D}(p, \theta) = \int d\phi \sum_i \sum_{m, \Omega, \eta} \left| \sum_j \left(\sum_\tau \widetilde{b}^i_{\zeta, \eta}(p; \tau) \right) \cdot D^j_{m, \Omega}(\theta, \phi) \right|^2$$

(23)

We integrate over ϕ since there is no dependency on this angle.

References

[1] M. Born, R. Oppenheimer, Zur quantentheorie der molekeln, Ann. Phys. 389 (20) (1927) 457–484.
[2] A.G. Suits, Invited review article: photofragment imaging, Rev. Sci. Instrum. 89 (11) (2018) 111101.
[3] V.S. Batista, M.T. Zanni, B.J. Greenblatt, D.M. Neumark, W.H. Miller, Femtosecond photoelectron spectroscopy of the i 2- anion: a semiclassical molecular dynamics simulation method, J. Chem. Phys. 110 (8) (1999) 3736–3747.
[4] R.N. Zare, Photoejection dynamics, Mol. Photochem 4 (1) (1972) 1–37.
[5] S.E. Choi, R.B. Bernstein, Theory of oriented symmetric-top molecule beams: Precession, degree of orientation, and photofragmentation of rotationally state-selected molecules, J. Chem. Phys. 85 (1) (1986) 150–161.
[6] T. Seideman, The analysis of magnetic-state-selected angular distributions: a quantum mechanical form and an asymptotic approximation, Chem. Phys. Lett. 253 (3–4) (1996) 279–285.
[7] P. Wang, A. Sayler, K. Carnes, J. Xia, M. Smith, B. Esry, I. Ben-Itzhak, Dissociation of h 2+ in intense femtosecond laser fields studied by coincidence three-dimensional momentum imaging, Phys. Rev. A 74 (4) (2006) 043411.
[8] F. Anis, B. Esry, Role of nuclear rotation in dissociation of h 2+ in a short laser pulse, Phys. Rev. A 77 (3) (2008) 033416.
[9] J. McKenna, F. Anis, A. Sayler, B. Gaire, N.G. Johnson, E. Parke, K. Carnes, B. Esry, I. Ben-Itzhak, Controlling strong-field fragmentation of h 2+ by temporal effects with few-cycle laser pulses, Phys. Rev. A 85 (2) (2012) 023405.
[10] A. Csehi, M. Kowalewski, G.J. Halász, Á. Vibók, Ultrafast dynamics in the vicinity of quantum light-induced conical intersections, New J. Phys. 21 (9) (2019) 093040.
[11] Z. Sun, C. Wang, W. Zhao, C. Yang, Mapping of the light-induced conical intersections in the photoelectron spectra of k2 molecules, Spectrochim. Acta Part A Mol. Biomol. Spectrosc. 207 (2019) 348–353.
[12] M. McDonald, B. McGuyer, F. Apfelbeck, C.-H. Lee, I. Majewska, R. Moszynski, T. Zelevinsky, Photodissociation of ultracold diatomic strontium molecules with quantum state control, Nature 535 (7610) (2016) 122–126.
[13] G.J. Halász, Á. Vibók, L.S. Cederbaum, Direct signature of light-induced conical intersections in diatomics, J. Phys. Chem. Lett. 6 (3) (2015) 348–354.
[14] P. Badankó, G.J. Halász, L.S. Cederbaum, Á. Vibók, A. Csehi, Communication: Substantial impact of the orientation of transition dipole moments on the dynamics of diatomics in laser fields, J. Chem. Phys. 149 (18) (2018) 181101.
[15] A. Shahi, Y. Albeck, D. Strasser, Intense-field multiple-detachment of f2: Competition with photodissociation, J. Phys. Chem. A 121 (16) (2017) 3037–3044.
[16] A. Shahi, Y. Albeck, D. Strasser, Ultrafast f2- photodissociation by intense laser pulses: a time-resolved fragment imaging study, in: EPJ Web Conf., vol. 205, EDP

Sciences, 2019, p. 09012.
[17] R.N. Zare, Angular Momentum: Understanding Spatial Aspects in Chemistry and Physics, J. Wiley & Sons, 1988.
[18] Y. Band, S. Kallush, R. Baer, Rotational aspects of short-pulse population transfer in diatomic molecules, Chem. Phys. Lett. 392 (1–3) (2004) 23–27.
[19] R. Kosloff, H. Tal-Ezer, A direct relaxation method for calculating eigenfunctions and eigenvalues of the schrödinger equation on a grid, Chem. Phys. Lett. 127 (3) (1986) 223–230.
[20] H. Tal-Ezer, R. Kosloff, An accurate and efficient scheme for propagating the time dependent schrödinger equation, J. Chem. Phys. 81 (9) (1984) 3967–3971.
[21] R. Kosloff, Propagation methods for quantum molecular dynamics, Ann. Rev. Phys. Chem. 45 (1) (1994) 145–178.
[22] R. Chen, H. Guo, The chebyshev propagator for quantum systems, Comput. Phys. Commun. 119 (1) (1999) 19–31.
[23] D. Kosloff, R. Kosloff, A fourier method solution for the time dependent schrödinger equation as a tool in molecular dynamics, J. Comput. Phys. 52 (1) (1983) 35–53.
[24] R. Kosloff, Time-dependent quantum-mechanical methods for molecular dynamics, J. Phys. Chem. 92 (8) (1988) 2087–2100.
[25] A.T. Eppink, D.H. Parker, Velocity map imaging of ions and electrons using electrostatic lenses: Application in photoelectron and photofragment ion imaging of molecular oxygen, Rev. Sci. Instrum. 68 (9) (1997) 3477–3484.
[26] G. Ashkenazi, U. Banin, A. Bartana, R. Kosloff, S. Ruhman, Quantum description of the impulsive photodissociation dynamics of i3- in solution, Adv. Chem. Phys. 100 (1997) 229–316.
[27] R. Kosloff, A.D. Hammerich, D. Tannor, Excitation without demolition: Radiative excitation of ground-surface vibration by impulsive stimulated raman scattering with damage control, Phys. Rev. Lett. 69 (15) (1992) 2172.
[28] I.M. Robert Moszynski, Private ccmmunication.
[29] A. Tóth, P. Badankó, G.J. Halász, Á. Vibók, A. Csehi, Importance of the lowest-lying πelectronic state in the photodissociation dynamics of lif, Chem. Phys. 515 (2018) 418–426.
[30] S. Kallush, S. Fleischer, Orientation dynamics of asymmetric rotors using random phase wave functions, Phys. Rev. A 91 (6) (2015) 063420.
[31] Y. Liu, S.L. Horton, J. Yang, J.P.F. Nunes, X. Shen, T.J. Wolf, R. Forbes, C. Cheng, B. Moore, M. Centurion, et al., Spectroscopic and structural probing of excited-state molecular dynamics with time-resolved photoelectron spectroscopy and ultrafast electron diffraction, Phys. Rev. X 10 (2) (2020) 021016.
[32] R. Kosloff, D. Kosloff, Absorbing boundaries for wave propagation problems, J. Comput. Phys. 63 (2) (1986) 363–376.
[33] J. Muga, J. Palao, B. Navarro, I. Egusquiza, Complex absorbing potentials, Phys. Rep. 395 (6) (2004) 357–426.